

1 **Formaldehyde evolution in U.S. wildfire plumes during FIREX-**

2 **AQ**

3

4 Jin Liao<sup>1,2</sup>, Glenn M. Wolfe<sup>1</sup>, Reem A. Hannun<sup>1,3</sup>, Jason M. St. Clair<sup>1,3</sup>, Thomas F. Hanisco<sup>1</sup>,  
5 Jessica B. Gilman<sup>4</sup>, Aaron Lamplugh<sup>4,5</sup>, Vanessa Selimovic<sup>6</sup>, Glenn S. Diskin<sup>7</sup>, John B. Nowak<sup>7</sup>,  
6 Hannah S. Halliday<sup>8</sup>, Joshua P. DiGangi<sup>7</sup>, Samuel R. Hall<sup>9</sup>, Kirk Ullmann<sup>9</sup>, Christopher D.  
7 Holmes<sup>10</sup>, Charles H. Fite<sup>10</sup>, Anxhelo Agastra<sup>10</sup>, Thomas B. Ryerson<sup>4,\*</sup>, Jeff Peischl<sup>4,5</sup>, Ilann  
8 Bourgeois<sup>4,5</sup>, Carsten Warneke<sup>4</sup>, Matthew M. Coggon<sup>4,5</sup>, Georgios I. Gkatzelis<sup>4,5,\*\*</sup>, Kanako  
9 Sekimoto<sup>11</sup>, Alan Fried<sup>12</sup>, Dirk Richter<sup>12</sup>, Petter Weibring<sup>12</sup>, Eric C. Apel<sup>9</sup>, Rebecca S. Hornbrook<sup>9</sup>,  
10 Steven S. Brown<sup>4</sup>, Caroline C. Womack<sup>4,5</sup>, Michael A. Robinson<sup>4,5</sup>, Rebecca A. Washenfelder<sup>4</sup>,  
11 Patrick R. Veres<sup>4</sup>, J. Andrew Neuman<sup>4,5</sup>

12  
13 <sup>1</sup>Atmospheric Chemistry and Dynamics Laboratory, NASA Goddard Space Flight Center, Greenbelt, MD, USA

14 <sup>2</sup>Universities Space Research Association, Columbia, MD, USA

15 <sup>3</sup>Joint Center for Earth Systems Technology, University of Maryland Baltimore County, Baltimore, MD, USA

16 <sup>4</sup>NOAA Chemical Science Laboratory (CSL), Boulder, CO, USA

17 <sup>5</sup>Cooperative Institute for Research in Environmental Science (CIRES), University of Colorado, Boulder, CO, USA

18 <sup>6</sup>Department of Chemistry, University of Montana, Missoula, MT, USA

19 <sup>7</sup>NASA Langley Research Center, Hampton, VA, USA

20 <sup>8</sup>Environmental Protection Agency, Durham, NC, USA

21 <sup>9</sup>Atmospheric Chemistry Observations & Modeling Laboratory, National Center for Atmospheric Research, Boulder,  
22 CO, USA

23 <sup>10</sup>Earth, Ocean and Atmospheric Science, Florida State University, FL, USA

24 <sup>11</sup>Yokohama City University, Japan

25 <sup>12</sup>Institute of Arctic and Alpine Research (INSTAAR), University of Colorado, Colorado, USA.

26 \*now at Scientific Aviation, Boulder, Colorado, USA.

27 \*\*now at Forschungszentrum Jülich GmbH, Jülich, Nordrhein-Westfalen, DE, Germany.

28  
29 *Correspondence to:* Jin Liao (jin.liao@nasa.gov)

30 **Abstract.** Formaldehyde (HCHO) is one of the most abundant non-methane volatile organic compounds (VOCs)  
31 emitted by fires. HCHO also undergoes chemical production and loss as a fire plume ages, and it can be an important  
32 oxidant precursor. In this study, we disentangle the processes controlling HCHO by examining its evolution in wildfire  
33 plumes sampled by the NASA DC-8 during the FIREX-AQ field campaign. In nine of the twelve analyzed plumes,  
34 dilution-normalized HCHO increases with physical age (range 1 – 6 h). The balance of HCHO loss (mainly via  
35 photolysis) and production (via OH-initiated VOC oxidation) seems to control the sign and magnitude of this trend.  
36 Plume-average OH concentrations, calculated from VOC decays, range from  $-0.5 (\pm 0.5) \times 10^6$  to  $5.3 (\pm 0.7) \times 10^6$   
37 cm<sup>-3</sup>. The production and loss rates of dilution-normalized HCHO seem to decrease with plume age. Plume-to-plume  
38 variability in dilution-normalized secondary HCHO production correlates with OH abundance rather than normalized  
39 OH reactivity, suggesting that OH is the main driver of fire-to-fire variability in HCHO secondary production.  
40 Analysis suggests an effective HCHO yield of  $0.33 (\pm 0.05)$  per VOC molecule oxidized for the 12 wildfire plumes.  
41 This finding can help connect space-based HCHO observations to the oxidizing capacity of the atmosphere and to  
42 VOC emissions.

43

44 **1. Introduction**

45 Wildfire biomass burning is a large source of trace gases and aerosols that affect regional atmospheric chemistry,  
46 human health, air quality, radiative balance and climate. Wildfire frequency and intensity are expected to increase  
47 with global warming under higher temperatures and drier conditions in the future (Westerling et al., 2006). Wildfire  
48 emissions of volatile organic compounds (VOCs) are a complex mixture spanning orders of magnitude in  
49 concentration, reactivity, and volatility (Gilman et al., 2015; Koss et al., 2018). These VOCs contribute to increased  
50 regional tropospheric ozone (Alvarado et al., 2010; Jaffe and Wigder, 2012; Mauzerall et al., 1998; Wotawa and  
51 Trainer, 2000) and can deposit onto or evaporate from organic aerosols in biomass burning air masses (Garofalo et al.,  
52 2019; Majdi et al., 2019; Palm et al., 2020).

53

54 Formaldehyde (HCHO) is one of the most abundant non-methane VOCs emitted by wildfires (Akagi et al., 2011;  
55 Gilman et al., 2015; Simpson et al., 2011). HCHO emissions vary with total carbon emissions, modified combustion  
56 efficiency (MCE) and fuel type. Emission factors of HCHO decrease as MCE increases (e.g., Liu et al., 2017;  
57 Yokelson et al., 1999), indicating that more HCHO is produced from smoldering fires than from flaming fires. HCHO  
58 emissions can vary by more than a factor of 2 among tropical forest, savanna, boreal forest and temperate forest biomes  
59 (Akagi et al., 2011). In addition to direct emissions, HCHO is formed in fire plumes via VOC oxidation. Alvarado et  
60 al. (2020) used TROPOMI data to show that HCHO enhancements in wildfire plumes persist for days downwind.  
61 HCHO also serves as an important source of peroxy radicals ( $\text{HO}_2$ ), thereby influencing the formation of ozone and  
62 other secondary pollutants (Yokelson et al., 1999).

63

64 Few studies have investigated the photochemical evolution of HCHO in biomass burning plumes, and these studies  
65 have reported both net HCHO production and loss. Mauzerall et al. (1998) reported average HCHO enhancement  
66 ( $\Delta\text{HCHO}/\Delta\text{CO}$ ) of 9.5 ppt/ppb for fresh plumes (less than 0.5 day), 1.8 ppt/ppb for recent plumes (less than 1 day),  
67 2.3 ppt/ppb for aged plumes (< 5 days old), and 0.9 ppt/ppb for old plumes (>5 days old). Trentmann et al. (2005)  
68 observed a potential increasing trend of  $\Delta\text{HCHO}/\Delta\text{CO}$  from 20 ppt/ppb to over 30 ppt/ppb with limited data and  
69 simulated a flat trend of  $\Delta\text{HCHO}/\Delta\text{CO}$  within 1 h age since emission from a Savanna fire plume in Africa. Müller et  
70 al. (2016) also observed an increasing trend of  $\Delta\text{HCHO}/\Delta\text{CO}$  with an average of 22.7 ppt/ppb and simulated a flat or  
71 slightly decreasing trend of  $\Delta\text{HCHO}/\Delta\text{CO}$  in a small fresh agricultural biomass burning plume in Georgia, US. While  
72 such case studies are valuable, we lack a general understanding of the drivers of plume trends and plume-to-plume  
73 variability in HCHO evolution.

74

75 HCHO is also one of the few VOCs that can be observed from space, and the global coverage of satellite observations  
76 has been leveraged to provide insights into a variety of atmospheric chemistry questions. HCHO is correlated with  
77 organic aerosols in biomass burning air masses, and this correlation might be exploited to estimate organic aerosol  
78 abundance from satellite HCHO measurements (Liao et al., 2019). In regions with constant or very high OH reactivity,  
79 HCHO variability is closely linked to OH variability (Valin et al., 2016; Wolfe et al., 2019) and may be used to infer  
80 OH. Satellite HCHO columns have also been widely used to constrain emissions of isoprene and other VOCs (Fu et

81 al., 2007; Kaiser et al., 2018; Marais et al., 2014; Millet et al., 2008; Stavrakou et al., 2009). Understanding the  
82 emissions, chemistry and trends of HCHO in wildfires will facilitate the application of satellite HCHO towards broad-  
83 scale wildfire smoke processes and impacts.

84  
85 The Fire Influence on Regional to Global Environments and Air Quality experiment (FIREX-AQ) deployed a  
86 comprehensive suite of instruments aboard the NASA DC-8 aircraft to study wildfires and agricultural fires in the US.  
87 It provided a great opportunity to systematically study the emissions and chemistry of HCHO in wildfire plumes. In  
88 the following, we describe the HCHO dependence on plume age in wildfire plumes from FIREX-AQ, assess the  
89 drivers of HCHO trends, and examine the factors controlling variability in secondary HCHO production.

90  
91 **2. Methods**

92 **2.1 FIREX-AQ field campaign and measurements description**

93 During FIREX-AQ, a combination of four aircraft (the NASA DC-8, NASA ER-2, and two NOAA Twin Otters)  
94 with a comprehensive suite of in situ and remote sensing instruments were deployed to characterize fire emissions  
95 and chemistry with operational bases in Boise, ID and Salina, KS from July to September 2019. This study focuses  
96 on wildfire plumes sampled by the NASA DC-8 aircraft during FIREX-AQ.

97  
98 In situ HCHO observations were acquired by several instruments onboard the DC-8; here we primarily use  
99 measurements from the In Situ Airborne Formaldehyde (ISAF) instrument (Cazorla et al., 2015). ISAF uses laser-  
100 induced fluorescence to detect HCHO. A tunable UV laser excites HCHO molecules to an excited electronic state and  
101 the resulting fluorescence is detected with a photon-counting photomultiplier tube. The laser wavelength is modulated  
102 on and off a rotational absorption feature (353.163 nm), and the difference between the “online” and “offline” signals  
103 is proportional to the HCHO concentration.

104  
105 ISAF was calibrated pre- and post-mission with a compressed-gas HCHO cylinder ( $584 \pm 15$  ppbv in nitrogen, Air  
106 Liquide). Sensitivity typically varies by less than 5% between calibrations. Flow meters for the standard dilution  
107 system were calibrated against a DryCal calibrator (Mesa Labs) with an accuracy of  $> 99\%$ . The HCHO standard  
108 concentration was calibrated before and after the field deployment with an MKS Multigas 2031 Fourier transform  
109 infrared spectrometer. Gas standard mixing ratios are typically reproducible to within 2% of the mean value measured  
110 over multiple years. IR-determined mixing ratios are adjusted by a factor of 0.96 based on a separate long-path UV  
111 absorption experiment (Cazorla et al., 2015). Thus, ISAF HCHO mixing ratios are ultimately tied to the UV cross  
112 sections of Meller and Moortgat (2000) as recommended by the JPL 2011 evaluation (Sander et al., 2011). The  
113 detection limit of ISAF was 30 pptv for 1-Hz data at signal/noise = 1 and the accuracy of ISAF HCHO measurements  
114 was estimated as  $10\% + 10$  pptv. The  $1/e$  response time of ISAF during FIREX-AQ was about 300 ms, limited mainly  
115 by flow through the sample cell.

117 During FIREX-AQ, ISAF HCHO measurements correlated with those from the Compact Atmospheric Multispecies  
118 Spectrometer (CAMS) (Richter et al., 2015), with a coefficient of determination  $r^2$  of 0.99, a slope of 1.27 (CAMS vs.  
119 ISAF), and a near-zero intercept for 1-Hz average wildfire data from equally weighted orthogonal distance regression  
120 (Fig. S1). The systematic bias between the CAMS and ISAF measurements exceeds the combined stated uncertainty  
121 (10% for ISAF, 6% for CAMS). Post-mission comparisons suggest this discrepancy is due to the absolute calibration  
122 of compressed-gas HCHO standards, which are tied to literature-recommended UV (ISAF) or IR (CAMS) cross  
123 sections; the source of this discrepancy is still under investigation. Remotely-sensed HCHO column retrievals rely on  
124 the same UV cross sections (De Smedt et al., 2018) that are used to calibrate the ISAF instrument. The HCHO  
125 enhancements in the plumes (Sect 3.1) and the estimated effective yield of HCHO from VOC oxidation by OH (Sect.  
126 3.3) can have a potential low bias of 27% due to the ISAF and CAMS HCHO measurement difference. This uncertainty  
127 proportionally affects quantitative analysis results but does not alter qualitative conclusions.

128

129 We also use several supporting measurements in our analysis. CO was measured via mid-IR wavelength modulation  
130 spectroscopy by the Differential Absorption Carbon Monoxide Measurement (DACOM) instrument (Sachse et al.,  
131 1991). Photolysis rates were derived from the Actinic flux measurements by the Charged-coupled device Actinic Flux  
132 Spectroradiometer (CAFS) (Hall et al., 2018). Alkenes were measured by the NOAA Whole Air Sampler (iWAS)  
133 (Lerner et al., 2017). Ozone ( $O_3$ ) measurements were from the NOAA Chemiluminescence instrument (Bourgeois et  
134 al., 2020). OH reactivity calculations used VOCs measurements from the NOAA Proton-Transfer Reaction Time-of-  
135 Flight Mass Spectrometry (PTR-ToF-MS) (Yuan et al., 2016), NCAR Trace Organic Gas Analyzer (TOGA) (Apel et  
136 al., 2015) outfitted with a Time-of-Flight Mass Spectrometer, NOAA Airborne Cavity Enhanced Spectrometer (ACES)  
137 (Min et al., 2016), and NOAA Iodide Ion Time-of-Flight (ToF) Chemical Ionization Mass Spectrometer (CIMS)  
138 (Veres et al., 2020), listed in Table S1. Our analysis uses in situ measurements that are merged to the iWAS sampling  
139 period, which ranged from 1-9 seconds per canister, such that multiple samples were often acquired within a single  
140 plume crossing.

141

## 142 **2.2 Normalized excess mixing ratio (NEMR) and physical age definitions**

143 NEMR is defined as the difference between the concentration of species X in the plume and in the background air  
144 outside of the plume, normalized by the difference between CO concentrations in the plume and the background  
145 outside of the plume. Because photochemical production of CO is very small compared to the high CO concentrations  
146 in the biomass burning plumes (e.g., CO production from HCHO photolysis and oxidation for 1 h is about 2.5 ppbv,  
147 which is < 1% of CO concentrations of 985 ppbv on average in the plumes), trace gases concentrations are normalized  
148 to CO in the biomass burning plumes to account for dilution, as in many previous biomass burning studies (e.g., Müller  
149 et al., 2016; Selimovic et al., 2019).

$$150 \text{ NEMR} = \frac{\Delta X}{\Delta CO} \quad (1)$$

151 The background air outside of the plumes was manually selected and could be different or the same for different  
152 transects of the same plume, depending on the availability of the iWAS data. The HCHO NEMR is denoted by nHCHO  
153 below.

154

155 Physical age was estimated using a Lagrangian trajectory analysis (Holmes et al., in preparation) and described briefly  
156 here. Fire source locations were pinpointed using the MODIS/ASTER Airborne Simulator (MASTER) instrument  
157 data onboard the DC-8. Upwind trajectories from aircraft locations were computed and the advection age was  
158 calculated from the time when a trajectory was closest to the fire. Plume rise time from the surface to the trajectory  
159 initialization altitude assumed a vertical wind speed of 7 m/s. The smoke age is the sum of advection age plus rise age  
160 averaged over several meteorological models. The average uncertainty of the estimated physical age for the analyzed  
161 wildfire plumes was 37% with an interquartile range of 20% based on the range of ages derived from the High-  
162 Resolution Rapid Refresh (HRRR), North American Mesoscale Forecast System (NAM) CONUS Nest, and Global  
163 Forecast System (GFS 0.25°) meteorological datasets.

164

### 165 **2.3 Plume selection**

166 Details about the specific selected wildfire plumes among all sampled wildfire plumes during FIREX-AQ are provided  
167 in Table S2. Wildfire plumes that meet the conditions listed below are above the background HCHO concentrations,  
168 which typically vary from 100 ppt – 1 ppb during FIREX-AQ, and are selected to study the evolution of HCHO in  
169 wildfires.

170 a) Lagrangian sampling pattern

171 Lagrangian sampling patterns are defined as flight tracks intercepted the plumes with flight leg directions  
172 approximately perpendicular to the horizontal wind directions and more than three transects downwind with different  
173 distances from the fire.

174 b) Appropriate VOC decay for the period analyzed with sufficient data samples

175 We selected the plume samples where chemical age correlated with physical age. This was defined by a coefficient of  
176 determination  $r^2 \geq 0.57$  for a plot of  $\ln(\text{trans-2-butene/propene})$  or  $\ln(\text{cis-2-butene/propene})$  vs physical age. We used  
177 2-butenes/propene as chemical age tracers in this analysis because these gases have comparable lifetimes to physical  
178 age for most of the analyzed plumes. We filtered out plume data if the correlation coefficient of  $\ln(\text{trans-2-}$   
179  $\text{butene/propene})$  or  $\ln(\text{cis-2-butene/propene})$  vs. physical age degraded at older physical ages. Figure S2 shows  
180  $\ln(\text{trans-2-butene/propene})$  and  $\ln(\text{cis-2-butene/propene})$  vs. physical age for the plumes that satisfied conditions a)  
181 and had iWAS data available. The threshold of  $r^2 = 0.57$  is chosen by visual inspection of all VOC decay in Fig. S2.  
182 We also filtered out plumes with total number of data points  $< 8$  in the iWAS sample periods for an entire selected  
183 circuit of multiple plume transects with good VOC decay. Due to the inhomogeneity of the plumes, too few data points  
184 can introduce large bias. In the analyzed plume periods,  $\ln(\text{trans-2-butene/propene})$  or  $\ln(\text{cis-2-butene/propene})$  also  
185 has good correlations with the maleic anhydride/furan ratio (Fig. S3), another tracer of chemical age in biomass  
186 burning plumes (Coggon et al., 2019; personal communication with Carsten Warneke and Matthew M. Coggon, 2021).

187 The Mica and Lick Creek plume on 02 August 2019 is the plume with the least number of data points among the  
188 selected plumes (N = 8).

189

190 The above filters, applied to a total of 26 fire plumes, yield 11 daytime plumes and 1 nighttime plume that are  
191 suitable for our analysis (Table S2). The nighttime plume on 12 August was after 8:00 pm local time with average  
192 O<sub>3</sub> photolysis rate of essentially zero. One of the twelve plumes (Blackwater) occurred in the southeast US and the  
193 remaining 11 plumes were in the western US.

194

## 195 **2.4 Estimating average OH concentrations in the plumes**

196 Plume photochemical age is estimated based on the relative decay of primary emitted VOCs that have different  
197 reaction rate coefficients with OH (e.g., Warneke et al., 2007). We can estimate the average concentration of OH by  
198 combining the photochemical age with the trajectory-based air mass age. Cis-2-butene/propene ratios and trans-2-  
199 butene/propene ratios are used to estimate OH in this analysis because these gases have lifetimes comparable to  
200 physical age (2–6 h) for most of the analyzed plumes and using two VOC ratios help reduce the uncertainty. The  
201 lifetimes of propene, cis-2-butene, and trans-2-butene are approximately 4.5 h, 2.3 h, and 1.8 h, respectively, at OH  
202 concentrations of 2 × 10<sup>6</sup> molecules cm<sup>-3</sup> (Atkinson et al., 2006). Because both 2-butenes also differ from propene in  
203 O<sub>3</sub> reaction rate coefficients, the reactions of these alkenes with O<sub>3</sub> are also considered when we estimate the OH  
204 concentrations. We assume that the variability in the butenes–propene relationship is driven by OH and O<sub>3</sub> and that  
205 there is negligible change in the relative emission ratios over the sampled plumes. Different slopes in cis-2-  
206 butene/propene and trans-2-butene/propene vs plume age (Fig. S2) depend on the differences in reaction rate  
207 coefficients of OH and O<sub>3</sub> with 2-butene (cis-2-butene and trans-2-butene) and propene, in addition to OH and O<sub>3</sub>  
208 concentrations, as shown in Eq. (2). These reaction rate coefficients are those reported by Atkinson et al. (2006) with  
209 real time temperature and pressure dependence. The plumes average reaction rate coefficients are  $k_{\text{propene,OH}} =$   
210  $3.1 \times 10^{-11} \text{ cm}^3 \text{ molecule}^{-1} \text{ s}^{-1}$ ,  $k_{\text{cis-2-butene,OH}} = 6.4 \times 10^{-11} \text{ cm}^3 \text{ molecule}^{-1} \text{ s}^{-1}$ ,  $k_{\text{trans-2-butene,OH}} = 8.0 \times 10^{-11} \text{ cm}^3$   
211  $\text{molecule}^{-1} \text{ s}^{-1}$ ,  $k_{\text{propene,O}_3} = 6.4 \times 10^{-18} \text{ cm}^3 \text{ molecule}^{-1} \text{ s}^{-1}$ ,  $k_{\text{cis-2-butene,O}_3} = 9.9 \times 10^{-17} \text{ cm}^3 \text{ molecule}^{-1} \text{ s}^{-1}$ , and  
212  $k_{\text{trans-2-butene,O}_3} = 1.5 \times 10^{-16} \text{ cm}^3 \text{ molecule}^{-1} \text{ s}^{-1}$ .

$$213 \ln \frac{\text{butene}}{\text{propene}} = \ln \frac{\text{butene}_0}{\text{propene}_0} - \{(k_{\text{butene+OH}} - k_{\text{propene+OH}})[\text{OH}] + (k_{\text{butene+O}_3} - k_{\text{propene+O}_3})[\text{O}_3]\}t \quad (2)$$

214 OH concentrations are derived from the slope of  $\ln \frac{\text{butene}}{\text{propene}}$  vs.  $t$  (physical age), the measured ozone concentrations  
215 and the reaction rate coefficients.

$$217 [\text{OH}] = \frac{\text{slope}_{\text{butene}} + (k_{\text{butene+O}_3} - k_{\text{propene+O}_3})[\text{O}_3]}{k_{\text{propene+OH}} - k_{\text{butene+OH}}} \quad (3)$$

218 Because the instantaneous O<sub>3</sub> measurements do not reflect the oxidation history, the average ozone concentration of  
219 the entire circuit with multiple transects is used to represent the integrated O<sub>3</sub> effect on alkene oxidation. The  
220 uncertainty due to O<sub>3</sub> variation and the uncertainty in the slope of  $\ln \frac{\text{butene}}{\text{propene}}$  vs.  $t$  are propagated to estimate the total

221 uncertainty in plume-average OH. Butene in Eq. (2) and (3) represents trans-2-butene or cis-2-butene, both of which  
222 are used in average OH estimation. O<sub>3</sub> variation, uncertainty in OH due to O<sub>3</sub> variation, total OH uncertainty, and  
223 estimated OH are listed in Table S3.

224

## 225 **2.5 Calculating primary HCHO normalized mixing ratios and secondary HCHO production rates**

226 To understand the relative importance of primary emission vs. secondary production of HCHO in fire plumes  
227 downwind, we calculate primary and secondary HCHO as the plume ages. The primary HCHO time profile is  
228 calculated by the following equation:

$$229 \quad nHCHO_{\text{primary}} = nHCHO_0 \exp(-J_{HCHO} + k_{HCHO}[\text{OH}])t \quad (4)$$

230 where  $nHCHO_0$  is equal to the fitted observed  $nHCHO$  (HCHO NEMR) closest to the fire source,  $J_{HCHO}$  is the measured  
231 HCHO photolysis frequency in iWAS sample periods averaged and interpreted in physical age space,  $k_{HCHO}$  is the  
232 reaction rate coefficient between HCHO and OH, and  $t$  is the physical age.  $nHCHO_{\text{secondary}}$  is calculated by subtracting  
233  $nHCHO_{\text{primary}}$  from the measured  $nHCHO$ . Here we assumed the fitted observed  $nHCHO$  closest to the fire source is  
234 equal to  $nHCHO$  at the emission source. This assumption will not impact the secondary  $nHCHO$  production rate  
235 calculated below.

236

237 To characterize secondary HCHO production in wildfire plumes, we calculate the secondary  $nHCHO$  production rate.

238 The secondary  $nHCHO$  production rate is derived from the HCHO mass balance equation.

$$239 \quad \frac{dHCHO}{dt} = P - L - D \quad (5)$$

240 where  $P$  is chemical production,  $L$  is chemical loss, and  $D$  is dilution. The calculation of the secondary  $nHCHO$   
241 production rate is shown in Eq. (6). The derivation of Eq. (6) from Eq. (5) can be found in Appendix A.

$$242 \quad \frac{P}{\Delta CO} \text{ (or } \frac{d nHCHO}{dt} \text{)} = \frac{dnHCHO}{dt} + (J_{HCHO} + k_{HCHO}[\text{OH}])nHCHO. \quad (6)$$

243 Here,  $\frac{dnHCHO}{dt}$  is taken as the slope of measured  $nHCHO$  vs physical age and other parameters are as defined above.

244

## 245 **2.6 Impact of potential variation in HCHO emission ratios on $nHCHO$ trend**

246 In this analysis, we assume the variability in the HCHO/CO emission ratio (that is,  $nHCHO$  at the source) is much  
247 smaller than the variability in  $nHCHO$  induced by chemistry for any single fire plume. Emission factors of both HCHO  
248 and CO (that is, g of gas per kg of fuel burned) depend on MCE, fuel type, and other factors (e.g., Liu et al., 2017;  
249 Yokelson et al., 1999). Normalizing HCHO by CO removes the strong negative dependence of HCHO emission factors  
250 on MCE. A small positive trend of  $nHCHO$  vs. MCE is due to higher  $nHCHO$  and MCE for the eastern US wildfire  
251 plume than the western US wildfire plumes (Fig. S4). No clear trend of MCE in  $nHCHO$  plume evolution was observed  
252 in FIREX-AQ data (Fig. S5). Emissions of CO<sub>2</sub> correlate with fire radiative power (FRP) detected by satellite during  
253 FIREX-AQ, and the variability of FRP could affect the variability of downwind concentrations (Wiggins et al., 2020).  
254 We found that HCHO correlates with CO<sub>2</sub> (Fig. S6a) and thus likely also with FRP because the change of measured

255 CO<sub>2</sub> correlates with the change of FRP (Wiggins et al., 2020). To account for emission variation and dilution, which  
256 are main factors affecting the absolute concentrations of trace gases and aerosols in the plumes, HCHO is normalized  
257 to CO to investigate the impact of photochemistry on HCHO evolution in the plumes. Photochemistry takes place  
258 while emission varies. When normalized to CO, nHCHO does not strongly depend on CO<sub>2</sub> (Fig. S6b and Fig. S7) or  
259 FRP. FRP and MCE do not control the trends of nHCHO.

260

## 261 **2.7 OH reactivity calculation**

262 We calculate the observed OH reactivity using the Framework for 0-D Atmospheric Modeling (F0AM v4) (Wolfe et  
263 al., 2016) with the Master Chemical Mechanism v3.3.1 (MCM; Jenkin et al., 2015) and additional chemical reactions  
264 from recent publications of newly-observed biomass burning species and reactions (Coggon et al., 2019; Decker et al.,  
265 2019). The VOC chemical species included in the F0AM model are listed in Table S1. We calculate the OH-VOC  
266 reactivity ( $\sum k_i VOC_i$ ) by excluding OH reactions with NO<sub>2</sub> and CO from the total OH reactivity and define the  
267 normalized OH-VOC reactivity or normalized total OH reactivity as OH-VOC reactivity normalized by CO or total  
268 OH reactivity normalized by CO.

269

## 270 **3. Results and discussion**

### 271 **3.1 OH concentration estimation**

272 OH is the main oxidant that reacts with VOCs to produce HCHO in the daytime. As described in Sect. 2.4, we estimate  
273 plume-average OH concentrations using the relative decays of 2-butenes to propene via Eq. (3). The decay of the  
274 natural logarithm of the trans-2-butene to propene ratio and the cis-2-butene to propene ratio with physical age is  
275 plotted in Fig. S2. Figure S2 includes all the plumes that meet selection condition (a) in Sect. 2.3, 12 plumes of which  
276 with good correlations ( $r^2 = 0.57\text{--}0.99$ ) between 2-butenes/propene and plume age and sufficient data (data points  $>$   
277 8) are selected for this analysis. The lowest correlation coefficient of the selected plumes occurs for the nighttime  
278 plume on 12 August 2019 and the daytime plume on 29 July 2019. This indicates that the photochemical age of these  
279 plumes is consistent with their physical age, and the oxidation chemistry can be reasonably represented by average  
280 OH and O<sub>3</sub>. The slopes in Fig. S2 infer the estimated OH concentrations and their coefficients of determination ( $r^2$ )  
281 imply how good the VOC decay can be used to estimate OH.

282

283 The estimated average OH concentrations for the 12 plumes are shown in Fig. 1. The uncertainties in OH  
284 concentrations are based on the standard error in the slope of ln(butenes/propene) vs physical age and the standard  
285 deviation of O<sub>3</sub> concentrations. The average and standard deviation of O<sub>3</sub> concentrations and the uncertainty in OH  
286 estimation due to the impact of O<sub>3</sub> standard deviation are listed in Table S3. Plume-to-plume variability in average  
287 OH concentrations is generally consistent between the two ratio methods. OH concentrations from trans-2-butene  
288 are systematically higher than those from cis-2-butene by 27% on average, which may reflect systematic bias in

289 reaction rate coefficients or observations. For all plumes where both calculations were available, differences are  
290 within the combined uncertainties. The average OH concentrations from trans-2-butene to propene and cis-2-butene  
291 to propene were used to represent the average OH concentrations of the plumes. The average OH concentrations  
292 covered a large range, varying from  $-0.5(\pm 0.5) \times 10^6$  (for a nighttime plume) to  $5.3(\pm 0.7) \times 10^6$  molecules cm $^{-3}$ .

293

### 294 **3.2 Trends of HCHO in wildfire plumes**

295 nHCHO in wildfire plumes can increase or decrease as plumes age. The trends of measured nHCHO vs. physical age  
296 and the corresponding quadratic polynomial regression for 12 selected plumes are plotted in Fig. 2. Quadratic  
297 polynomial regression is used because it has suitable degrees of freedom to capture the trends. Considering the CO  
298 measurement uncertainty of  $\leq 7\%$  and HCHO measurement uncertainty of 10%, the uncertainty of nHCHO is  
299 estimated to be  $\pm 12\%$  with a potential systematic low bias of as much as 27% (based on the difference between ISAF  
300 and CAMS). Random error due to HCHO and CO measurement precision is negligible when averaging over the iWAS  
301 integration time in high-concentration biomass burning plumes.

302

303 In the absence of secondary production, we expect nHCHO to decay with a time constant of a few hours in the daytime.  
304 The blue curves in Fig. 2 show the predicted decay of initial nHCHO using observed HCHO photolysis rates and  
305 measurement-derived OH concentrations. Because the variability in nHCHO in one transect is significant, we use the  
306 start point of the observed nHCHO fitted curve to represent the observed nHCHO closest to fire. HCHO photolysis  
307 frequencies are averaged generally over each transect and linearly interpolated to determine continuous age-dependent  
308 photolysis frequencies. The calculated nHCHO without production is higher than primary (emitted) nHCHO because  
309 some HCHO production and loss had already occurred before the closest transect.

310

311 The fraction of primary and secondary nHCHO varies from plume to plume and depends on secondary HCHO  
312 production rates and total HCHO loss rates. This can be inferred from nHCHO trends and the loss-only nHCHO  
313 decays in Fig. 2 and is also shown in Fig. S8. We estimate the fraction of primary HCHO by assuming nHCHO and  
314 the loss rate of nHCHO are constant between emission and the closest observation. The primary HCHO fraction could  
315 decay rapidly to be 60% in about 1 h of aging or it could decay slowly to still account for 60% in about 5h of aging.  
316 The primary and secondary fractions of HCHO indicate the impact of direct emission and photochemistry on the fire  
317 plume composition downwind. The slowing down increase in secondary nHCHO fraction with time probably indicate  
318 that the production of secondary nHCHO slows down with physical age. The average and standard deviation of  
319 nHCHO production and loss rates for each plume are provided in Table S4.

320

321 HCHO production exceeds loss in 9 of the 12 selected plumes, indicated by overall positive trends of nHCHO vs.  
322 physical age in Fig. 2. Plumes exhibiting overall negative nHCHO trends (20190725 Shady 2, 20190803 Williams  
323 Flats 1 and 20190806 Williams Flats) have higher overall nHCHO loss rates than production rates (Table S4). This  
324 shows that fire-to-fire variability in the overall nHCHO trend relates to the balance between loss (via photolysis) and

325 production (via VOC oxidation). HCHO loss by photolysis can be either higher or lower than the loss by reaction with  
326 OH, but on average photolysis is faster. HCHO loss via photolysis accounts for  $63 \pm 27\%$  of the total HCHO loss in  
327 daytime plumes. The average HCHO lifetime by photolysis was  $8.2 (\pm 8.8)$  h for the 11 daytime plumes, shorter than  
328 the average HCHO lifetime by OH oxidation of  $23.5 (\pm 31.3)$  h. For some plume transects, there was significant  
329 variability in HCHO photolysis frequencies over iWAS averaging intervals due to the aerosol radiative effects.  
330 Applying filters to only analyze the data with relatively homogeneous in-plume HCHO photolysis rates does not alter  
331 our conclusions. Plume-average OH is not well correlated with the HCHO photolysis frequency (Fig. S9), likely due  
332 to inter-fire variability of OH sources and sinks.

333

334 Besides the variability among different plumes, nHCHO production and loss also vary within a plume across physical  
335 age. In all analyzed plumes, nHCHO slope shifts from positive to neutral or negative within the first 2-6 h (Fig. 2).  
336 Figure S10 shows the age progression of nHCHO production, loss, and net change for the 12 plumes. In general, both  
337 production and loss decrease with age. Decreases in both are expected due to declining solar radiation, which results  
338 from the typical late-afternoon FIREX-AQ sampling strategy. Reduced production with increasing age may also  
339 reflect the decay of reactive VOC and oxidant precursors (e.g., HONO).

340

### 341 **3.3 Controls on secondary HCHO formation**

342 The secondary HCHO production rate is determined by a mass balance approach with loss, production, and dilution  
343 terms, as discussed in Sect. 2.5. The average secondary nHCHO production rate correlates with the average OH  
344 concentration ( $r^2 = 0.69$ , Fig. 3a). The secondary production rates of nHCHO were calculated from the trends of  
345 observed nHCHO ( $\frac{dnHCHO}{dt}$ ), photolysis loss rate and OH (Eq. 6). Although OH concentrations are used to calculate  
346 secondary nHCHO production rates, the nHCHO loss term ( $k[OH]nHCHO$ ) due to OH only accounts for 2–35% of  
347 all the terms on the righthand side of Eq. (6), which is used to calculate secondary nHCHO production rate for the  
348 plumes. This indicates that the good correlation between secondary nHCHO production rate and OH is not due to the  
349 inclusion of OH in nHCHO production rate calculation. The uncertainty in nHCHO secondary production rates for  
350 each plume is estimated from the standard deviation of the calculated nHCHO secondary production rates along the  
351 physical age of the plume. The uncertainty in estimated OH is determined by the propagated uncertainties of OH from  
352 trans-2-butene to propene ratios and cis-2-butene to propene ratios. The nHCHO secondary production rates also  
353 correlate with the HCHO photolysis ( $r^2 = 0.53$  uncertainty weighted linear regression), which is not unexpected as OH  
354 and  $J_{HCHO}$  positively correlate as well. The correlation between nHCHO secondary production rates with oxidant ozone  
355 is poor ( $r^2 = 0.1$  from bivariate regression). The good correlations ( $r^2 = 0.69$ ) between the secondary production rate  
356 of nHCHO and average OH indicate that the variability in OH is a key driver of the secondary production rate of  
357 nHCHO. Although there is only one eastern US wildfire plume sampled during FIREX-AQ, it has high VOCs,  
358 nHCHO, nHCHO production rate, and OH, and the inclusion of the eastern US wildfire increase the coefficient of  
359 determination ( $r^2$  from 0.54 to 0.69) and the slope (m from 0.30 to 0.33) of nHCHO secondary production rates vs.  
360 OH. More wildfire sampling is needed to understand the difference between western and eastern US wildfires.

361  
362 Figure 3a is color-coded with normalized OH-VOC reactivity calculated from measured VOCs (Sect. 2.7). Plume-  
363 average normalized OH-VOC reactivity ranges from 11 to 31  $\text{s}^{-1}$  (ppm CO) $^{-1}$ , which is about 20% lower than  
364 normalized total OH reactivity across the analyzed plumes. nHCHO production rates vs. normalized OH-VOC  
365 reactivity (Fig. S11a) shows a lower coefficient of determination ( $r^2$ ) and a higher p value than Fig. 3a. Because  
366 uncertainty weighted linear regression yields a low  $r^2 = 0.08$  for Fig. S11a, unweighted (or equally weighted) bivariate  
367 linear regression is used. P-values in Fig. 3 show the correlation between nHCHO production rate vs. OH ( $p = 0.004$ )  
368 or vs. OH  $\times$  normalized OH-VOC reactivity ( $p = 0.003$ ) is statistically significant ( $p < 0.05$ ). Because the yield of  
369 HCHO from VOC oxidation is calculated in the study, normalized OH-VOC reactivity instead of normalized total OH  
370 reactivity is mainly used. A plot of nHCHO production rate vs. normalized total OH reactivity color coded with OH  
371 is shown in Fig. S11b. Similar to Fig. S11a, the correlation between nHCHO production rate with normalized total  
372 OH reactivity is also not significant. Because nHCHO trend, OH concentration, and normalized OH-VOC reactivity  
373 all depend on physical age, in addition to the different properties of the plumes, the difference in physical age among  
374 these plumes also has an impact on the average values.  
375

376 Figure 3b shows nHCHO production vs. the product of OH and dilution-normalized observed OH-VOC reactivity  
377 (averaged for each plume). The latter is a lower limit for the total average OH loss/production rate as observations do  
378 not include all OH sinks. The correlation is slightly higher than that in Fig. 3a because variability in normalized OH-  
379 VOC reactivity plays a smaller role than OH in affecting  $P_{\text{nHCHO}}$ . The slope of this relationship,  $0.33 \pm 0.05$ , is a metric  
380 for the effective yield of HCHO from OH-initiated VOC oxidation. Assuming that reaction of OH with a VOC is the  
381 rate-limiting step and ignoring non-OH sources, integrated HCHO production can be written as in Eq. (7).  
382

$$P_{\text{HCHO}} = \sum \alpha_i k_i [\text{OH}] [X_i] = \alpha_{\text{eff}} k'_{\text{OH}} [\text{OH}] \quad (7)$$

383 Where  $\alpha_i$  is the yield of HCHO from OH oxidation of any VOC reactant  $X_i$  and depends on both the structure of  $X$   
384 and the fate of reactive intermediates like peroxy radicals,  $k_i$  is the reaction rate coefficient for  $\text{VOC}_i + \text{OH}$ ,  $k'_{\text{OH}}$   
385 represents OH-VOC reactivity, and  $\alpha_{\text{eff}}$  is the effective yield weighted over OH-VOC reactions. If all OH reactivity  
386 (including reactions with CO and  $\text{NO}_2$ ) instead of OH-VOC reactivity is considered,  $\alpha_{\text{eff}}$  will be about 20% smaller.  
387 As discussed by Valin et al. (2016),  $\alpha_{\text{eff}}$  from all OH reactivity is expected to range from 0.2 to 0.4 depending on the  
388 magnitude of  $\text{NO}_x$  and the magnitude and speciation of VOC. The yield reported here (0.28 for all OH reactivity) is  
389 on the low end of this range, implying that HCHO production in the plumes is not very efficient due to the nature of  
390 the emitted VOC and/or the balance of  $\text{RO}_2$  reactions with  $\text{NO}$ ,  $\text{HO}_2$ , and other  $\text{RO}_2$ . High  $\alpha_{\text{eff}}$  values reported by  
391 Valin et al. (2016) occur in high isoprene emission regions, implying the emitted VOCs in wildfires are not as  
392 efficient as isoprene in producing HCHO. Our  $\alpha_{\text{eff}}$  of 0.28, when considering all OH reactivity, is higher than the  
393 value of 0.20 ( $\pm 0.01$ ) derived by Wolfe et al. (2019) for total-column HCHO in the remote troposphere, where  
394 methane oxidation is the primary HCHO source. The potential low bias in observed HCHO could lead to a  
395 proportional (27%) low bias in  $\alpha_{\text{eff}}$ . Species that are highly reactive and present in large quantities such as  $\text{CH}_3\text{CHO}$   
396 are important for OH-VOC reactivity and  $\alpha_{\text{eff}}$  calculation. We use PTRMS  $\text{CH}_3\text{CHO}$  data in OH-VOC reactivity

397 calculation because they are more easily integrated over the iWAS sampling time than TOGA CH<sub>3</sub>CHO. This  
398 indicates that besides the potential missing VOCs, the uncertainties in measured VOCs concentrations and different  
399 sampling time resolutions can also contribute to the uncertainties in OH reactivity and  $\alpha_{eff}$ . The  $\alpha_{eff}$  for the one  
400 eastern US wildfire plume is higher than that of the western US wildfire plumes but more sampling of eastern  
401 wildfire plumes is needed to determine if there is a statistical difference in  $\alpha_{eff}$ . Higher NO<sub>x</sub>/VOC ratio in the eastern  
402 than western US wildfire plumes may contribute to the higher  $\alpha_{eff}$  because more NO<sub>x</sub> generally means more radical  
403 turnover and a larger fraction of RO<sub>2</sub> + NO, both of which favor HCHO production.

404

#### 405 **3.4 Implications for interpretation of satellite observations**

406 The quantification of the evolution of HCHO in wildfire plumes can be leveraged to enhance interpretations of satellite  
407 remote sensing observations. The good correlation of dilution-corrected secondary HCHO production and oxidant  
408 levels suggests the use of satellite HCHO data to estimate oxidant levels in biomass burning plumes. Similar to the  
409 studies of NO<sub>2</sub> lifetime from satellite NO<sub>2</sub> data (e.g., Laughner and Cohen, 2019; Liu et al., 2016), with parameterized  
410 production rates of HCHO as a function of OH from this study, the effective lifetime of HCHO and OH concentrations  
411 in the wildfire plumes could potentially be derived from remote sensing HCHO and CO data if the photolysis rates  
412 can be properly parameterized. Satellite HCHO retrievals in biomass burning plumes remain challenging, and  
413 information about vertical distributions of trace gases and aerosols from airborne measurements are likely needed to  
414 improve satellite retrievals in biomass burning plumes. The effective yield of HCHO from this analysis indicates that  
415 the biomass burning VOCs could be less efficient than isoprene in producing HCHO, although other factors such as  
416 balance of RO<sub>2</sub> reactions with NO, HO<sub>2</sub>, and other RO<sub>2</sub> can play a role. This information may be useful for estimating  
417 VOC emissions from satellite HCHO data.

418

#### 419 **4. Conclusions**

420 We studied the chemical evolution of HCHO in wildfire plumes during FIREX-AQ. Twelve well-developed plumes  
421 with consistent chemical and physical age 1–6 h downwind were selected among 26 wildfire plumes sampled. During  
422 plume transport and aging, dilution-corrected HCHO increased in smoke from nine wildfires and decreased in three,  
423 depending on the balance of HCHO production and loss processes. Secondary nHCHO production tracks average OH  
424 concentrations, indicating that the variability in OH rather than the variability in the reactive VOC pool drives the  
425 production of nHCHO in these wildfire plumes. The effective HCHO yield from OH-initiated VOC oxidation is  
426 estimated to be 0.33 ( $\pm 0.05$ ), which is about in the middle of previous studies of isoprene-rich, urban VOC-dominated  
427 and remote atmospheric background regions.

428 **Appendix A. Derivation of secondary nHCHO production rate from mass balance equation**

429 Change of HCHO concentration with time can be obtained from mass balance equation (Eq. A1)

430 
$$\frac{d \text{HCHO}}{dt} = P - L - D \quad (\text{A1})$$

431 where P is the HCHO chemical production term; L is the HCHO chemical loss term; and D is the dilution term.

432 Considering the HCHO normalized excess mixing ratio ( $n\text{HCHO} = \frac{\text{HCHO} - \text{HCHO}_{\text{bkg}}}{\text{CO} - \text{CO}_{\text{bkg}}}$ ) and assuming that the HCHO

433 background change is relatively small ( $\frac{d \text{HCHO}_{\text{bkg}}}{dt} \approx 0$ ),  $\frac{d \text{HCHO}}{dt}$  can be written as

434 
$$\frac{d \text{HCHO}}{dt} = \Delta \text{CO} \frac{d n\text{HCHO}}{dt} + n\text{HCHO} \frac{d \Delta \text{CO}}{dt}. \quad (\text{A2})$$

435 Because L, D and P terms are as

436 
$$L = (J_{\text{HCHO}} + k_{\text{HCHO}} [\text{OH}]) \text{HCHO}. \quad (\text{A3})$$

437 
$$D = -k_{\text{dil}}(\text{HCHO} - \text{HCHO}_{\text{bkg}}) = -\frac{1}{\Delta \text{CO}} \frac{d \Delta \text{CO}}{dt} \text{HCHO}.$$

438 
$$(A4)$$

439 
$$P = \frac{d \text{HCHO}}{dt} + L + D = \Delta \text{CO} \frac{d n\text{HCHO}}{dt} + n\text{HCHO} \frac{d \Delta \text{CO}}{dt} + (J_{\text{HCHO}} + k_{\text{HCHO}} [\text{OH}]) \text{HCHO} - \frac{1}{\Delta \text{CO}} \frac{d \Delta \text{CO}}{dt} \text{HCHO}. \quad (A5)$$

440 By assuming  $\text{HCHO} \gg \text{HCHO}_{\text{bkg}}$ ,  $\frac{P}{\Delta \text{CO}}$  can be written as

441 
$$\frac{P}{\Delta \text{CO}} = \frac{dn\text{HCHO}}{dt} + (J_{\text{HCHO}} + k_{\text{HCHO}} [\text{OH}]) n\text{HCHO}. \quad (A6)$$

442 Where  $\frac{d n\text{HCHO}}{dt}$  can be derived from measured HCHO and CO vs physical age;  $J_{\text{HCHO}}$  is the HCHO photolysis  
443 coefficient, derived from in-situ actinic flux measurements; OH is calculated from VOCs ratios (Sect.2.4);  $k_{\text{HCHO}}$  is  
444 the reaction rate coefficient of HCHO and OH.

445

446

447 **Data and code availability:**

448 Data are publicly available at <https://www-air.larc.nasa.gov/missions/firex-aq/index.html> with a dataset doi: [FIREX-AQ DOI: 10.5067/SUBORBITAL/FIREXAQ2019/DATA001](https://doi.org/10.5067/SUBORBITAL/FIREXAQ2019/DATA001). F0AM is available at <https://github.com/AirChem/F0AM>. Model setup scripts for this study are available from the contact author upon request.

449

450 **Author contribution:**

451 GMW and TFH directed the research direction. JL analyzed the data and discussed the results with GMW. JL wrote  
452 the manuscript. TFH, GMW, JMS, JL, and RAH made ISAF HCHO measurements. JBG, AL, and VS made iWAS  
453 measurements. GSD, JBN, HSH, JPG made DACOM CO measurements. SRH and KU made CAFS photolysis  
454 frequencies measurements. CDH, CHF, and AA provided the trajectories-based plume physical age. HSH provided  
455 MCE calculation. TBR, JP, and IB made O<sub>3</sub> measurements. CW, MMC, GIG, and KS made PTR-ToF-MS VOC

460 measurements. AF, DR, and PW made CAMS HCHO measurements. ECA and RSH made TOGA VOC  
461 measurements. SSB, CCW, MAR, and RAW made ACES measurements. PRV and JAN made CIMS measurements.  
462 All authors reviewed and commented on the manuscript.

463

464 **Competing interests:**

465 The authors declare that they have no conflict of interest.

466

467 **Acknowledgements:**

468 We gratefully acknowledge the crew, logistical personnel, science team and science leadership who facilitated the  
469 FIREX-AQ mission. We also thank Gao Chen and Ali Aknan for the merged DC8 dataset used in this study. JL,  
470 GMW, RAH, JMS, and TFH acknowledge support from the NASA Tropospheric Composition Program and NOAA  
471 Climate Program Office's Atmospheric Chemistry, Carbon Cycle and Climate (AC4) program (NA17OAR4310004).  
472 SRH and KU were funded by the NASA Tropospheric Composition Program (80NSSC18K0638). This material is  
473 based upon work supported by the National Center for Atmospheric Research, which is a major facility sponsored by  
474 the National Science Foundation under Cooperative Agreement No. 1852977. KS acknowledges the support from the  
475 fund a Grant-in-Aid for Scientific Research (C) (18K05179) from the Ministry of Education, Culture, Sports, Science  
476 and Technology of Japan.

477

478

479

480

481 **References**

482 Akagi, S. K., Yokelson, R. J., Wiedinmyer, C., Alvarado, M., Reid, J. S., Karl, T., Crounse, J. D., and Wennberg, P.  
483 O.: Emission Factors for Open and Domestic Biomass Burning for Use in Atmospheric Models, *Atmos. Chem.  
484 Phys.*, 11, 4039–4072, doi:10.5194/acp-11-4039-2011, 2011.

485 Alvarado, L. M. A., Richter, A., Vrekoussis, M., Hilboll, A., Kalisz Hedegaard, A. B., Schneising, O., and Burrows,  
486 J. P.: Unexpected long-range transport of glyoxal and formaldehyde observed from the Copernicus Sentinel-5  
487 Precursor satellite during the 2018 Canadian wildfires, *Atmos. Chem. Phys.*, 20(4), 2057–2072, doi:10.5194/acp-20-  
488 2057-2020, 2020.

489 Alvarado, M. J., Logan, J. A., Mao, J., Apel, E., Riemer, D., Blake, D., Cohen, R. C., Min, K. E., Perring, A. E.,  
490 Browne, E. C., Wooldridge, P. J., Diskin, G. S., Sachse, G. W., Fuelberg, H., Sessions, W. R., Harrigan, D. L.,  
491 Huey, G., Liao, J., Case-Hanks, A., Jimenez, J. L., Cubison, M. J., Vay, S. A., Weinheimer, A. J., Knapp, D. J.,  
492 Montzka, D. D., Flocke, F. M., Pollack, I. B., Wennberg, P. O., Kurten, A., Crounse, J., St. Clair, J. M., Wisthaler,  
493 A., Mikoviny, T., Yantosca, R. M., Carouge, C. C., and Le Sager, P.: Nitrogen oxides and PAN in plumes from  
494 boreal fires during ARCTAS-B and their impact on ozone: An integrated analysis of aircraft and satellite  
495 observations, *Atmos. Chem. Phys.*, 10(20), 9739–9760, doi:10.5194/acp-10-9739-2010, 2010.

496 Apel, E. C., Hornbrook, R. S., Hills, A. J., Blake, N. J., Barth, M. C., Weinheimer, A., Cantrell, C., Rutledge, S. A.,  
497 Basarab, B., Crawford, J., Diskin, G., Homeyer, C. R., Campos, T., Flocke, F., Fried, A., Blake, D. R., Brune, W.,  
498 Pollack, I., Peischl, J., Ryerson, T., Wennberg, P. O., Crounse, J. D., Wisthaler, A., Mikoviny, T., Huey, G., Heikes,  
499 B., Sullivan, D. O., and Riemer, D. D.: *J. Geophys. Res. Atmos.*, 120, 2505–2523,  
500 doi:10.1002/2014JD022121. Received, 2015.

501 Atkinson, R., Baulch, D. L., Cox, R. A., Crowley, J. N., Hampson, R. F., Hynes, R. G., Jenkin, M. E., Rossi, M. J.,  
502 Troe, J., and IUPAC Subcommittee: Evaluated kinetic and photochemical data for atmospheric chemistry: Volume  
503 II – gas phase reactions of organic species, *Atmos. Chem. Phys.*, 6, 3625–4055, doi:<https://doi.org/10.5194/acp-6-3625-2006>, 2006.

504 Bourgeois, I., Peischl, J., Thompson, C. R., Aikin, K. C., Campos, T., Clark, H., Commane, R., Daube, B., Diskin,  
505 G. W., Elkins, J. W., Gao, R. S., Gaudel, A., Hints, E. J., Johnson, B. J., Kivi, R., McKain, K., Moore, F. L.,  
506 Parrish, D. D., Querel, R., Ray, E., Sánchez, R., Sweeney, C., Tarasick, D. W., Thompson, A. M., Thouret, V.,  
507 Witte, J. C., Wofsy, S. C., and Ryerson, T. B.: Global-scale distribution of ozone in the remote troposphere from the  
508 ATom and HIPPO airborne field missions, *Atmos. Chem. Phys.*, 20(17), 10611–10635, doi:10.5194/acp-20-10611-  
509 2020, 2020.

510 Cazorla, M., Wolfe, G. M., Bailey, S. A., Swanson, A. K., Arkinson, H. L., and Hanisco, T. F.: A new airborne  
511 laser-induced fluorescence instrument for in situ detection of formaldehyde throughout the troposphere and lower  
512 stratosphere, *Atmos. Meas. Tech.*, 8(2), 541–552, doi:10.5194/amt-8-541-2015, 2015.

513 Coggon, M. M., Lim, C. Y., Koss, A. R., Sekimoto, K., Yuan, B., Gilman, J. B., Hagan, D. H., Selimovic, V.,  
514 Zarzana, K. J., Brown, S. S., M Roberts, J., Müller, M., Yokelson, R., Wisthaler, A., Krechmer, J. E., Jimenez, J. L.,  
515 Cappa, C., Kroll, J. H., de Gouw, J., and Warneke, C.: OH chemistry of non-methane organic gases (NMOGs)  
516 emitted from laboratory and ambient biomass burning smoke: Evaluating the influence of furans and oxygenated  
517

518 aromatics on ozone and secondary NMOG formation, *Atmos. Chem. Phys.*, 19(23), 14875–14899, doi:10.5194/acp-  
519 19-14875-2019, 2019.

520 Decker, Z. C. J., Zarzana, K. J., Coggon, M., Min, K. E., Pollack, I., Ryerson, T. B., Peischl, J., Edwards, P., Dubé,  
521 W. P., Markovic, M. Z., Roberts, J. M., Veres, P. R., Graus, M., Warneke, C., de Gouw, J., Hatch, L. E., Barsanti,  
522 K. C., and Brown, S. S.: Nighttime Chemical Transformation in Biomass Burning Plumes: A Box Model Analysis  
523 Initialized with Aircraft Observations, *Environ. Sci. Technol.*, 53(5), 2529–2538, doi:10.1021/acs.est.8b05359,  
524 2019.

525 Derek, Y.: Least-squares fitting of a straight line, *Can. J. Phys.*, 46(16), 1845–1847, doi:10.1139/p68-523, 1968.

526 Fu, T. M., Jacob, D. J., Palmer, P. I., Chance, K., Wang, Y. X., Barletta, B., Blake, D. R., Stanton, J. C., and Pilling,  
527 M. J.: Space-based formaldehyde measurements as constrains on volatile organic compound emissions in east and  
528 south Asia and implications for ozone, *J. Geophys. Res. Atmos.*, 112(6), 1–15, doi:10.1029/2006JD007853, 2007.

529 Garofalo, L. A., Pothier, M. A., Levin, E. J. T., Campos, T., Kreidenweis, S. M., and Farmer, D. K.: Emission and  
530 Evolution of Submicron Organic Aerosol in Smoke from Wildfires in the Western United States, *ACS Earth Space  
531 Chem.*, 3(7), 1237–1247, doi:10.1021/acsearthspacechem.9b00125, 2019.

532 Gilman, J. B., Lerner, B. M., Kuster, W. C., Goldan, P. D., Warneke, C., Veres, P. R., Roberts, J. M., de Gouw, J.  
533 A., Burling, I. R., and Yokelson, R. J.: Biomass burning emissions and potential air quality impacts of volatile  
534 organic compounds and other trace gases from fuels common in the US, *Atmos. Chem. Phys.*, 15(24), 13915–13938,  
535 doi:10.5194/acp-15-13915-2015, 2015.

536 Hall, S. R., Ullmann, K., Prather, M. J., Flynn, C. M., Murray, L. T., Fiore, A. M., Correa, G., Strode, S. A.,  
537 Steenrod, S. D., Lamarque, J. F., Guth, J., Josse, B., Flemming, J., Huijnen, V., Luke Abraham, N., and Archibald,  
538 A. T.: Cloud impacts on photochemistry: Building a climatology of photolysis rates from the Atmospheric  
539 Tomography mission, *Atmos. Chem. Phys.*, 18(22), 16809–16828, doi:10.5194/acp-18-16809-2018, 2018.

540 Jaffe, D. A. and Wigder, N. L.: Ozone production from wildfires: A critical review, *Atmos. Environ.*, 51, 1–10,  
541 doi:10.1016/j.atmosenv.2011.11.063, 2012.

542 Jenkin, M. E., Young, J. C., and Rickard, A. R.: The MCM v3.3.1 degradation scheme for isoprene, *Atmos. Chem.  
543 Phys.*, 15(20), 11433–11459, doi:10.5194/acp-15-11433-2015, 2015.

544 Kaiser, J., Jacob, D. J., Zhu, L., Travis, K. R., Fisher, J. A., González Abad, G., Zhang, L., Zhang, X., Fried, A.,  
545 Crounse, J. D., Clair, J. M. S., and Wisthaler, A.: High-resolution inversion of OMI formaldehyde columns to  
546 quantify isoprene emission on ecosystem-relevant scales: Application to the southeast US, *Atmos. Chem. Phys.*,  
547 18(8), 5483–5497, doi:10.5194/acp-18-5483-2018, 2018.

548 Koss, A. R., Sekimoto, K., Gilman, J. B., Selimovic, V., Coggon, M. M., Zarzana, K. J., Yuan, B., Lerner, B. M.,  
549 Brown, S. S., Jimenez, J. L., Krechmer, J., Roberts, J. M., Warneke, C., Yokelson, R. J., and de Gouw, J.: Non-  
550 methane organic gas emissions from biomass burning: Identification, quantification, and emission factors from PTR-  
551 ToF during the FIREX 2016 laboratory experiment, *Atmos. Chem. Phys.*, 18(5), 3299–3319, doi:10.5194/acp-18-  
552 3299-2018, 2018.

553 Laughner, J. and Cohen, R. C.: Direct observation of changing NO<sub>x</sub> lifetime in North American cities, *Science*  
554 366(6466), 723–727, 2019.

555 Lerner, B. M., Gilman, J. B., Aikin, K. C., Atlas, E. L., Goldan, P. D., Graus, M., Hendershot, R., Isaacman-  
556 Vanwertz, G. A., Koss, A., Kuster, W. C., Lueb, R. A., McLaughlin, R. J., Peischl, J., Sueper, D., Ryerson, T. B.,  
557 Tokarek, T. W., Warneke, C., Yuan, B., and de Gouw, J. A.: An improved, automated whole air sampler and gas  
558 chromatography mass spectrometry analysis system for volatile organic compounds in the atmosphere, *Atmos.*  
559 *Meas. Tech.*, 10(1), 291–313, doi:10.5194/amt-10-291-2017, 2017.

560 Liao, J., Hanisco, T. F., Wolfe, G. M., St. Clair, J., Jimenez, J. L., Campuzano-Jost, P., Nault, B. A., Fried, A.,  
561 Marais, E. A., Gonzalez Abad, G., Chance, K., Jethva, H. T., Ryerson, T. B., Warneke, C., and Wisthaler, A.:  
562 Towards a satellite formaldehyde - in situ hybrid estimate for organic aerosol abundance, *Atmos. Chem. Phys.*, 19,  
563 2765–2785, doi:10.5194/acp-2018-651, 2019.

564 Liu, F., Beirle, S., Zhang, Q., Dörner, S., He, K., and Wagner, T.: NO<sub>x</sub> lifetimes and emissions of cities and power  
565 plants in polluted background estimated by satellite observations, *Atmos. Chem. Phys.*, 16(8), 5283–5298,  
566 doi:10.5194/acp-16-5283-2016, 2016.

567 Liu, X., Huey, L. G., Yokelson, R. J., Selimovic, V., Simpson, I. J., Müller, M., Jimenez, J. L., Campuzano-Jost, P.,  
568 Beyersdorf, A. J., Blake, D. R., Butterfield, Z., Choi, Y., Crounse, J. D., Day, D. A., Diskin, G. S., Dubey, M. K.,  
569 Fortner, E., Hanisco, T. F., Hu, W., King, L. E., Kleinman, L., Meinardi, S., Mikoviny, T., Onasch, T. B., Palm, B.  
570 B., Peischl, J., Pollack, I. B., Ryerson, T. B., Sachse, G. W., Sedlacek, A. J., Shilling, J. E., Springston, S., St. Clair,  
571 J. M., Tanner, D. J., Teng, A. P., Wennberg, P. O., Wisthaler, A., and Wolfe, G. M.: Airborne measurements of  
572 western U.S. wildfire emissions: Comparison with prescribed burning and air quality implications, *J. Geophys. Res.*  
573 *Atmos.*, 122(11), 6108–6129, doi:10.1002/2016JD026315, 2017.

574 Majdi, M., Sartelet, K., Maria Lanzafame, G., Couvidat, F., Kim, Y., Chrit, M., and Turquety, S.: Precursors and  
575 formation of secondary organic aerosols from wildfires in the Euro-Mediterranean region, *Atmos. Chem. Phys.*,  
576 19(8), 5543–5569, doi:10.5194/acp-19-5543-2019, 2019.

577 Marais, E. A., Jacob, D. J., Guenther, A., Chance, K., Kurosu, T. P., Murphy, J. G., Reeves, C. E., and Pye, H. O. T.:  
578 Improved model of isoprene emissions in Africa using Ozone Monitoring Instrument (OMI) satellite observations of  
579 formaldehyde: Implications for oxidants and particulate matter, *Atmos. Chem. Phys.*, 14(15), 7693–7703,  
580 doi:10.5194/acp-14-7693-2014, 2014.

581 Mauzerall, D. L., Logan, J. A., Jacob, D. J., Anderson, B. E., Blake, D. R., Bradshaw, J. D., Heikes, B., Sachse, G.  
582 W., Singh, H., and Talbot, B.: Photochemistry in biomass burning plumes and implications for tropospheric ozone  
583 over the tropical South Atlantic, *J. Geophys. Res. Atmos.*, 103(D7), 8401–8423, doi:10.1029/97JD02612, 1998.

584 Meller, R. and Moortgat, G. K.: Temperature dependence of the absorption cross sections of formaldehyde between  
585 223 and 323 K in the wavelength range 225–375 nm, *J. Geophys. Res. Atmos.*, 105(D6), 7089–7101,  
586 doi:10.1029/1999JD901074, 2000.

587 Millet, D. B., Jacob, D. J., Boersma, K. F., Fu, T. M., Kurosu, T. P., Chance, K., Heald, C. L., and Guenther, A.:  
588 Spatial distribution of isoprene emissions from North America derived from formaldehyde column measurements by  
589 the OMI satellite sensor, *J. Geophys. Res. Atmos.*, 113(2), 1–18, doi:10.1029/2007JD008950, 2008.

590 Min, K. E., Washenfelder, R. A., Dubé, W. P., Langford, A. O., Edwards, P. M., Zarzana, K. J., Stutz, J., Lu, K.,  
591 Rohrer, F., Zhang, Y., and Brown, S.: A broadband cavity enhanced absorption spectrometer for aircraft

592 measurements of glyoxal, methylglyoxal, nitrous acid, nitrogen dioxide, and water vapor, *Atmos. Meas. Tech.*, 9(2),  
593 423–440, doi:10.5194/amt-9-423-2016, 2016.

594 Müller, M., Anderson, B. E., Beyersdorf, A. J., Crawford, J. H., Diskin, G. S., Eichler, P., Fried, A., Keutsch, F. N.,  
595 Mikoviny, T., Thornhill, K. L., Walega, J. G., Weinheimer, A. J., Yang, M., Yokelson, R. J., and Wisthaler, A.: In  
596 situ measurements and modeling of reactive trace gases in a small biomass burning plume, *Atmos. Chem. Phys.*,  
597 16(6), 3813–3824, doi:10.5194/acp-16-3813-2016, 2016.

598 Palm, B. B., Peng, Q., Fredrickson, C. D., Lee, B. H., Garofalo, L. A., Pothier, M. A., Kreidenweis, S. M., Farmer,  
599 D. K., Pokhrel, R. P., Shen, Y., Murphy, S. M., Permar, W. Hu, L., Campos, T. L., Hall, S. R., Ullmann, K. Zhang,  
600 X., Flocke, F., Fischer, E. V., and Thornton, J. A.: Quantification of organic aerosol and brown carbon evolution in  
601 fresh wildfire plumes, *P. Natl. Acad. Sci. USA*, 117 (47) 29469–29477, doi:10.1073/pnas.2012218117, 2020.

602 Yokelson, R. J., Goode, J. G., Ward, D. E., Susott, R. A., Babbitt, R. E., Wade, D. D., Bertschi, I., Griffith, D. W.  
603 T., and Hao, W. M: Emissions of formaldehyde, acetic acid, methanol, and other trace gases from biomass fires in  
604 North Carolina measured by airborne Fourier transform infrared spectroscopy, *J. Geophys. Res. Atmos.*, 104(D23),  
605 30109–30125, doi:10.1029/1999JD900817, 1999.

606 Richter, D., Weibring, P., Walega, J. G., Fried, A., Spuler, S. M., and Taubman, M. S.: CAMS - Compact  
607 atmospheric multi-species spectrometer, *Conf. Lasers Electro-Optics Eur. - Tech. Dig.*, 2015-Augus, 5–6,  
608 doi:10.1364/CLEO\_AT.2015.ATu4J.5, 2015.

609 Sachse, G. W., Collins, Jr., J. E., Hill, G. F., Wade, L. O., Burney, L. G., and Ritter, J. A.: Airborne tunable diode  
610 laser sensor for high-precision concentration and flux measurements of carbon monoxide and methane, *Meas.  
611 Atmos. Gases*, 1433(May 1991), 157, doi:10.1111/12.46162, 1991.

612 Sander, S. P., Abbatt, J., Barker, J. R., Burkholder, J. B., Friedl, R. R., Golden, D. M., Huie, R. E., Kolb, C. E.,  
613 Kurylo, M. J., Moortgat, G. K., Orkin, V. L., and Wine, P. H.: Chemical Kinetics and Photochemical Data for Use in  
614 Atmospheric Studies Evaluation Number 17, *JPL Publ. 10-6*, Jet Propul [online] Available from:  
615 <http://jpldataeval.jpl.nasa.gov/>, 2011.

616 Selimovic, V., Yokelson, R. J., McMeeking, G. R., and Coefield, S.: In-situ measurements of trace gases, PM, and  
617 aerosol optical properties during the 2017 NW US wildfire smoke event, *Atmos. Chem. Phys.*, 19, 3905-3926,  
618 doi:10.5194/acp-19-3905-2019, 2019, 2019.

619 Simpson, I. J., Akagi, S. K., Barletta, B., Blake, N. J., Choi, Y., Diskin, G. S., Fried, A., Fuelberg, H. E., Meinardi,  
620 S., Rowland, F. S., Vay, S. A., Weinheimer, A. J., Wennberg, P. O., Wiebring, P., Wisthaler, A., Yang, M.,  
621 Yokelson, R. J., and Blake, D. R.: Boreal forest fire emissions in fresh Canadian smoke plumes: C1-C10 volatile  
622 organic compounds (VOCs), CO<sub>2</sub>, CO, NO<sub>2</sub>, NO, HCN and CH<sub>3</sub>CN, *Atmos. Chem. Phys.*, 11(13), 6445–6463,  
623 doi:10.5194/acp-11-6445-2011, 2011.

624 De Smedt, I., Theys, N., Yu, H., Danckaert, T., Lerot, C., Compernolle, S., Van Roozendael, M., Richter, A.,  
625 Hilboll, A., Peters, E., Pedergnana, M., Loyola, D., Beirle, S., Wagner, T., Eskes, H., Van Geffen, J., Folkert  
626 Boersma, K., and Veefkind, P.: Algorithm theoretical baseline for formaldehyde retrievals from S5P TROPOMI and  
627 from the QA4ECV project, *Atmos. Meas. Tech.*, 11(4), 2395–2426, doi:10.5194/amt-11-2395-2018, 2018.

628 Stavrakou, T., Müller, J. F., De Smedt, I., Van Roozendael, M., Van Der Werf, G. R., Giglio, L., and Guenther, A.:

629 Global emissions of non-methane hydrocarbons deduced from SCIAMACHY formaldehyde columns through 2003–  
630 2006, *Atmos. Chem. Phys.*, 9(11), 3663–3679, doi:10.5194/acp-9-3663-2009, 2009.

631 Trentmann, J., Yokelson, R. J., Hobbs, P. V., Winterrath, T., Christian, T. J., Andreae, M. O., and Mason, S. A.: An  
632 analysis of the chemical processes in the smoke plume from a savanna fire, *J. Geophys. Res. D Atmos.*, 110(12), 1–  
633 20, doi:10.1029/2004JD005628, 2005.

634 Valin, L. C., Fiore, A. M., Chance, K., and Abad, G. G.: The role of OH production in interpreting the variability of  
635 CH<sub>2</sub>O columns in the southeast U.S., *J. Geophys. Res. Atmos.*, 121, 478–493, doi:10.1038/175238c0, 2016.

636 Veres, P. R., Andrew Neuman, J., Bertram, T. H., Assaf, E., Wolfe, G. M., Williamson, C. J., Weinzierl, B., Tilmes,  
637 S., Thompson, C. R., Thames, A. B., Schroder, J. C., Saiz-Lopez, A., Rollins, A. W., Roberts, J. M., Price, D.,  
638 Peischl, J., Nault, B. A., Møller, K. H., Miller, D. O., Meinardi, S., Li, Q., Lamarque, J. F., Kupc, A., Kjaergaard, H.  
639 G., Kinnison, D., Jimenez, J. L., Jernigan, C. M., Hornbrook, R. S., Hills, A., Dollner, M., Day, D. A., Cuevas, C.  
640 A., Campuzano-Jost, P., Burkholder, J., Paul Bui, T., Brune, W. H., Brown, S. S., Brock, C. A., Bourgeois, I., Blake,  
641 D. R., Apel, E. C., and Ryerson, T. B.: Global airborne sampling reveals a previously unobserved dimethyl sulfide  
642 oxidation mechanism in the marine atmosphere, *Proc. Natl. Acad. Sci. U. S. A.*, 117(9), 4505–4510,  
643 doi:10.1073/pnas.1919344117, 2020.

644 Warneke, C., McKeen, S. A., de Gouw, J. A., Goldan, P. D., Kuster, W. C., Holloway, J. S., Williams, E. J., Lerner,  
645 B. M., Parrish, D. D., Trainer, M., Fehsenfeld, F. C., Kato, S., Atlas, E. L., Baker, A., and Blake, D. R.:  
646 Determination of urban volatile organic compound emission ratios and comparison with an emissions database, *J.  
647 Geophys. Res. Atmos.*, 112(10), doi:10.1029/2006JD007930, 2007.

648 Westerling, A. L., Hidalgo, H. G., Cayan, D. R., and Swetnam, T. W.: Warming and earlier spring increase Western  
649 U.S. forest wildfire activity, *Science* (80-), 313(5789), 940–943, doi:10.1126/science.1128834, 2006.

650 Wiggins, E. B., Soja, A. J., Gargulinski, E., Halliday, H. S., Pierce, R. B., Schmidt, C. C., Nowak, J. B., DiGangi, J.  
651 P., Diskin, G. S., Katich, J. M., Perring, A. E., Schwarz, J. P., Anderson, B. E., Chen, G., Crosbie, E. C., Jordan, C.,  
652 Robinson, C. E., Sanchez, K. J., Shingler, T. J., Shook, M., Thornhill, K. L., Winstead, E. L., Ziembka, L. D., and  
653 Moore, R. H.: High Temporal Resolution Satellite Observations of Fire Radiative Power Reveal Link Between Fire  
654 Behavior and Aerosol and Gas Emissions, *Geophys. Res. Lett.*, 47(23), doi:10.1029/2020GL090707, 2020.

655 Wolfe, G. M., Marvin, M. R., Roberts, S. J., Travis, K. R., and Liao, J.: The framework for 0-D atmospheric  
656 modeling (F0AM) v3.1, *Geosci. Model Dev.*, 9(9), 3309–3319, doi:10.5194/gmd-9-3309-2016, 2016.

657 Wolfe, G. M., Nicely, J. M., Clair, J. M. S., Hanisco, T. F., Liao, J., Oman, L. D., Brune, W. B., Miller, D., Thames,  
658 A., Abad, G. G., Ryerson, T. B., Thompson, C. R., Peischl, J., McKain, K., Sweeney, C., Wennberg, P. O., Kim, M.,  
659 Crounse, J. D., Hall, S. R., Ullmann, K., Diskin, G., Bui, P., Chang, C., and Dean-Day, J.: Mapping hydroxyl  
660 variability throughout the global remote troposphere via synthesis of airborne and satellite formaldehyde  
661 observations, *Proc. Natl. Acad. Sci. USA.*, 116(23), 11171–11180, doi:10.1073/pnas.1908931116, 2019.

662 Wotawa, G. and Trainer, M.: The influence of Canadian forest fires on pollutant concentrations in the United States,  
663 *Science* (80-), 288(5464), 324–328, doi:10.1126/science.288.5464.324, 2000.

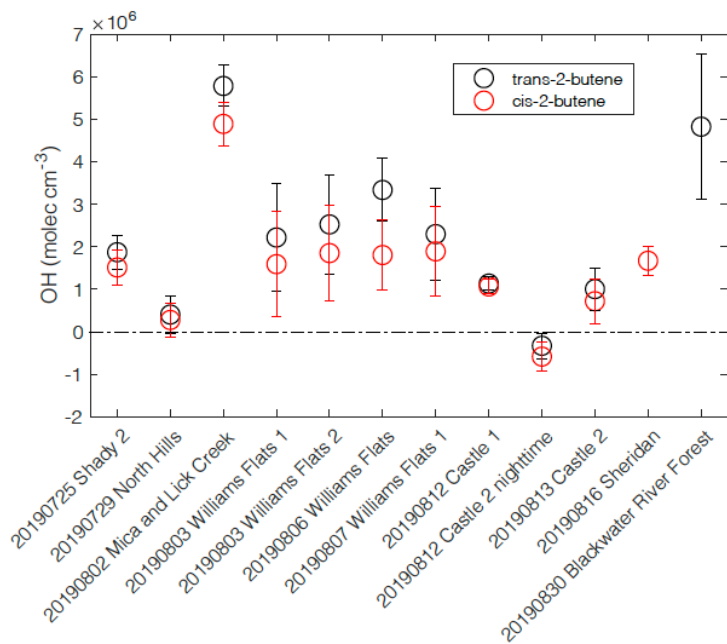
664 Yuan, B., Koss, A., Warneke, C., Gilman, J. B., Lerner, B. M., Stark, H., and de Gouw, J. A.: A high-resolution  
665 time-of-flight chemical ionization mass spectrometer utilizing hydronium ions (H<sub>3</sub>O<sup>+</sup> ToF-CIMS) for

666 measurements of volatile organic compounds in the atmosphere, *Atmos. Meas. Tech.*, 9(6), 2735–2752,  
667 doi:10.5194/amt-9-2735-2016, 2016.

668

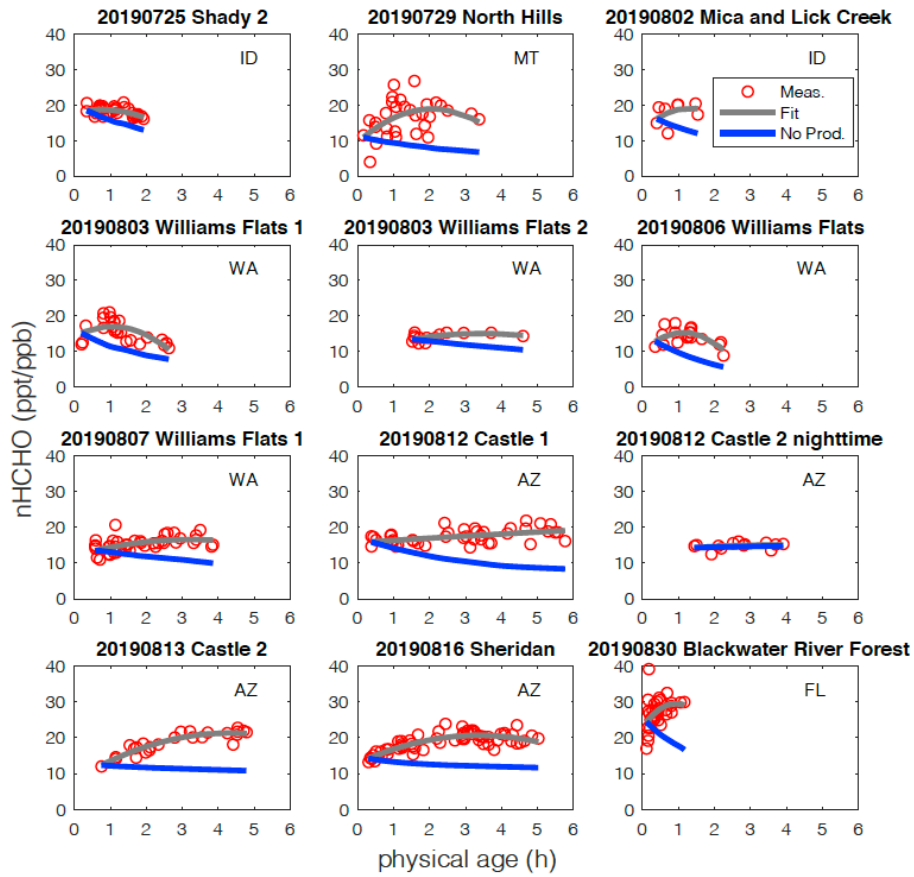
669

670 **Figures:**



671

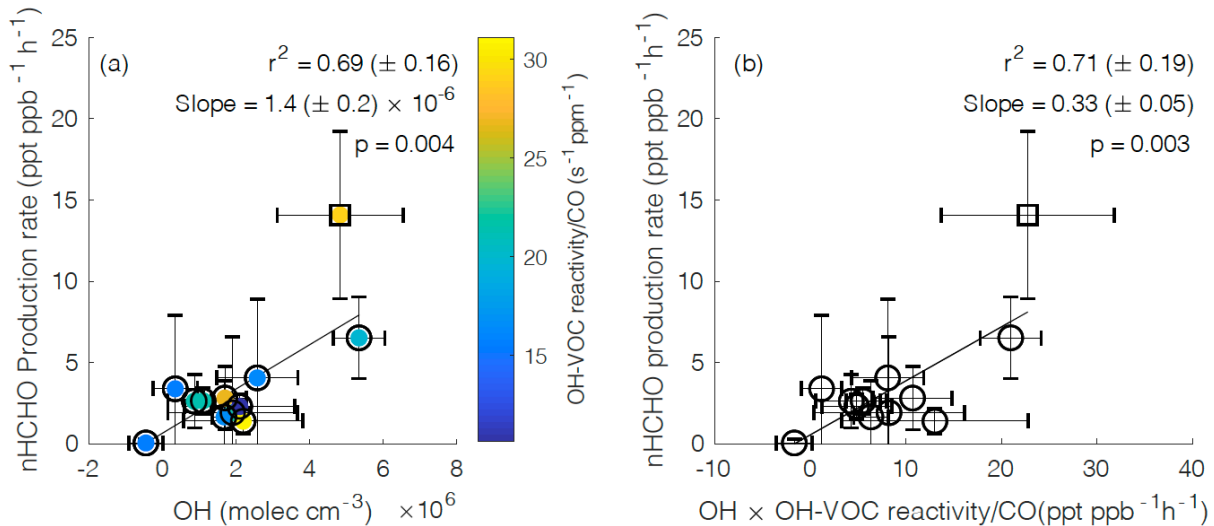
672 Figure 1. Estimated average OH concentrations for the plumes analyzed from the decay of trans-2-butene – propene  
673 (black) and the decay of cis-2-butene – propene (red). The error bars represent the propagated uncertainties from the  
674 slopes of butenes – propene decay and ozone variability within the plume.



675

676 Figure 2. Observed nHCHO (HCHO to CO NEMR) trends (red circle), quadratic polynomial fit (pink curve), and  
 677 calculated decay of nHCHO trend without secondary production (blue curve) using measured photolysis rates along  
 678 plume physical age for the 12 wildfire plumes. The state of fire location for each fire plume is listed.

679

680  
681

682 Figure 3. (a) Average secondary nHCHO production rate vs. average OH concentration, color-coded by normalized  
683 OH-VOC reactivity, for the 12 plumes including 11 western US wildfire plumes (circles) and 1 eastern US wildfire  
684 plume (square). An uncertainty weighted linear York regression (Derek, 1968) yields a slope =  $1.4 (\pm 0.2) \times 10^{-6}$  and  
685  $r^2 = 0.69 (\pm 0.16)$  for the 12 wildfire plumes. (b) Average secondary nHCHO production rate vs. the average product  
686 of OH and OH-VOC reactivity normalized to CO (OH  $\times$  OH-VOC reactivity/CO) for each plume. An uncertainty  
687 weighted linear York regression yields a slope =  $0.33 (\pm 0.05)$  and  $r^2 = 0.71 (\pm 0.19)$ . The slope represents the  
688 estimated effective yield  $\alpha_{eff}$  of HCHO per VOC molecule oxidized by OH for the US wildfires. The uncertainties in  
689  $r^2$  are from bootstrap analysis. The  $p$ -value in each panel is to evaluate if linear correlation is statistically significant  
690 ( $p < 0.05$ ).